NMR Imaging of Nonaqueous-Phase Liquid Dissolution in a Porous Medium

Christopher A. Baldwin and Lynn F. Gladden
Dept. of Chemical Engineering, University of Cambridge, Pembroke Street, Cambridge, CB2 3RA, U.K.

It is demonstrated how NMR imaging can be used noninvasively to quantify the volume of nonaqueous phase liquid (NAPL) present in an otherwise water-saturated porous medium. Data were recorded during the operation of a pump and treat (PT) remediation scheme on a bed of water-saturated sand contained within a vertical column. The model contaminant used was n-hexanol, and three different aqueous flow rates were employed. These data were then critically compared with the predictions of three models currently used to describe the dissolution of NAPL during a PT scheme: the linear mass-transfer model, the pore-diffusion model, and the shrinking-core model. The pore-diffusion model gave best agreement with the experimental data. However, none of the models predicted the observed dependence of mass transfer on Darcy velocity.

Introduction

Removal of a nonaqueous phase liquid (NAPL) from groundwater is often an important time-consuming task. Leaking gasoline storage tanks and ruptured hazardous waste disposal drums that discharge into nearby soil are prevalent threats to groundwater quality. NAPL that reaches the groundwater table becomes entrapped as small ganglia and, even if the solubility of the NAPL is very low (parts per thousand or million), a small volume of NAPL will contaminate a very large volume of groundwater and can do so over a long period of time (Freeze and Cherry, 1991). A common treatment for removing NAPLs in situ is pump and treat (PT). A PT process is a dissolution treatment where large volumes of water are flushed through the contaminated area, dissolving the contaminant more rapidly than natural flow rates would allow. Water is collected down-field and treated at the surface.

An aquifer contaminated with a NAPL is difficult to model because of the variety of conditions involved (in terms of the physical and chemical nature of the pore space and NAPL) and also a lack of fundamental understanding as to what phenomena are rate controlling in the mass transfer of the NAPL into the aqueous phase. A review of previous experimental studies investigating the dissolution of NAPLs within the saturated zone, and the various models for dissolution of NAPLs at residual saturation has recently been given by Imhoff et al. (1993). However, few experiments have so far been performed that allow direct observation of changing NAPL volume within a contaminated zone during the dissolution process. Geller and Hunt (1993) and Borden and Kao (1992) have reported changing effluent concentrations in transient experiments and, more recently, Imhoff et al. (1993) have used a gamma radiation technique to measure changing residual trichloroethylene (TCE) saturation in an otherwise water-saturated porous medium as clean water was flushed through the medium. Mass-transfer coefficients were computed and shown to be a function of Darcy velocity, TCE volumetric content, and distance into the region of residual TCE.

The lack of success in developing models of NAPL removal is largely due to the lack of information provided by current laboratory techniques describing the complex three-phase system under study. For example, laboratory research on dissolution of NAPLs from groundwater is typically performed in a small column containing sand and water into which an amount of NAPL is introduced, after which a dissolution period is commenced. As the treatment takes place, the outlet concentration of the contaminant is monitored and later used to evaluate a proposed mass-transfer model. The outlet concentration depends upon the saturation of NAPL (saturation in this context meaning fraction of void volume composed of NAPL) and the concentration of NAPL in the aqueous phase at all points before it in the column, thus its value is an extremely complex function of the multiphase system under study and provides little specific information about the dissolution process itself. In this work we report NMR imaging

experiments of a PT process, which provide NAPL saturation profiles along the length of the column during the course of NAPL removal. The NMR data are then compared with the predictions of three previously proposed models: the linear mass-transfer coefficient model (Powers et al., 1992); the pore-diffusion model (McDonald et al., 1993), and the shrinking-core model (Geller and Hunt, 1993). This study focuses on *n*-hexanol as the NAPL of interest. Darcy velocities in the range 0.64–6.37 cm/h were studied, and the time course of the NAPL removal was followed for several hours beyond the time at which residual saturation was obtained. For all Darcy velocities studied, the linear mass-transfer model gave poorest agreement with experimental data, while the pore diffusion model was seen to give best agreement with data. Further, regardless of the model considered, a significant increase in the rate of mass transfer was observed with increase in Darcy velocity, a result consistent with the observations reported by Imhoff et al. (1993).

MRI Theory

In the following paragraphs, a brief overview of the principles of nuclear magnetic resonance (NMR) imaging relevant to the present work is given. The interested reader will find a more detailed discussion in Gladden (1994); a rigorous treatment of the subject has been given by Callaghan (1991). NMR is exhibited by atomic nuclei that have a nonzero nuclear spin quantum number; in this work the spin-1/2 nucleus ^{1}H has been studied. When a sample containing such nuclei is placed in a static magnetic field, a net magnetization vector, $\boldsymbol{M}_0$, is induced within the system, which precesses about the applied magnetic field, $\boldsymbol{B}_0$, at an angular frequency given by

$$\omega_0 = \gamma B_0, \tag{1}$$

where ω_0 is known as the Larmor frequency and γ is the nuclear gyromagnetic ratio of the nucleus of interest. At equilibrium the net magnetization is aligned along the applied field, conventionally taken to be the z-axis, and is directly proportional to the total number of nuclei present (usually referred to as the *spin density*). To detect the NMR signal, the net magnetization vector, $\boldsymbol{M}_0$, must be rotated into the x, y-plane; this is achieved by applying a radio-frequency (RF) pulse at the Larmor frequency of the nucleus under study. The Larmor frequency of any given molecular species depends upon both the physical and chemical nature of the molecule, hence NMR is a molecule-specific probe. By irradiating a sample containing both water and hydrocarbon with a narrow-band rf pulse (known as a *soft pulse*), either one of the two species can be selectively excited, and thus quantitatively imaged.

In the NMR imaging experiment, the Larmor frequency of the nuclear spins under study is made dependent upon the position of each spin in the sample space by the application of a linear magnetic field gradient, $\boldsymbol{G}$, in addition to the large static magnetic field. The precessional frequency of spins in the sample is then related to the applied gradient by

$$\omega(\boldsymbol{r}) = \gamma B_0 + \gamma \boldsymbol{G}\cdot\boldsymbol{r}, \tag{2}$$

where $\boldsymbol{r}$ is the position vector of the spins within the sample. The signal, ds, obtained from the spins in an element of volume, dV, is then given by (Callaghan, 1991):

$$ds(\boldsymbol{G},t) = \rho(\boldsymbol{r})\exp[i\gamma(B_0 + \boldsymbol{G}\cdot\boldsymbol{r})t]dV, \tag{3}$$

where ρ is the spin density at position $\boldsymbol{r}$. A spatially resolved map of the spin density in the frequency domain is obtained from the time-domain signal by the Fourier transform:

$$\rho(\boldsymbol{r}) = \frac{1}{2\pi}\int\int\int s(\boldsymbol{k})\exp[-i2\pi\boldsymbol{k}\cdot\boldsymbol{r}]d\boldsymbol{k} \tag{4}$$

$$s(\boldsymbol{k}) = \int\int\int \rho(\boldsymbol{r})\exp[i2\pi\boldsymbol{k}\cdot\boldsymbol{r}]d\boldsymbol{r}, \tag{5}$$

where $\boldsymbol{k}$ is the reciprocal-space vector (Mansfield and Grannell, 1973) defined by

$$\boldsymbol{k} = \frac{1}{2\pi}\gamma\boldsymbol{G}t. \tag{6}$$

NMR imaging has been used by several workers to image two-phase flow of wetting and nonwetting phases in rock core samples (Chen et al., 1993; Fordham et al., 1993; Majors et al., 1990; and Roussel and Chardaire-Riviere, 1992). Majors et al. (1990) used an echo-time-encoded chemical shift imaging (CSI) technique to obtain spectral information for each image pixel, thus allowing quantification of both phases. In contrast, the other workers discriminated between the aqueous and organic phases by using deuterium oxide as the aqueous phase. Using this approach, ^{1}H imaging only obtains signals from the organic phase. In remediation experiments the use of D_2O to distinguish between hydrocarbon and aqueous phases is not practicable, since each experiment requires many pore volumes of the aqueous phase. Thus an alternative experimental approach must be adopted. In the present work the oil and water resonances were sufficiently well-resolved to allow the use of a water-suppression technique, which has the advantage over CSI of decreased acquisition time and a larger dynamic range, thereby enabling detection of lower NAPL concentrations. The larger dynamic range of the water-suppression technique can be understood by consideration of the spectral broadening effects that occur in the system of interest here. Spectral broadening arises because the water and NAPL exist within a sand matrix that causes a reduction in the T_2 of both the oil and water phases relative to their characteristic values in the respective pure states. Such broadening limits the ability of CSI techniques to study low NAPL concentrations because a low-intensity oil resonance will be overlapped by a broad water resonance of very much greater intensity; the CSI experiment probes both species within the same experiment. The pulse sequence used in the present study is illustrated in Figure 1, and takes the form of a spin-echo pulse train preceded by the SUBMERGE pulse, proposed by Doddrell et al. (1986), which suppresses the signal from the aqueous phase. Although not able to achieve this perfectly, the suppression of the water resonance allows the NAPL concentration to be studied to much lower values since the signal is not being observed against an overwhelming water resonance.

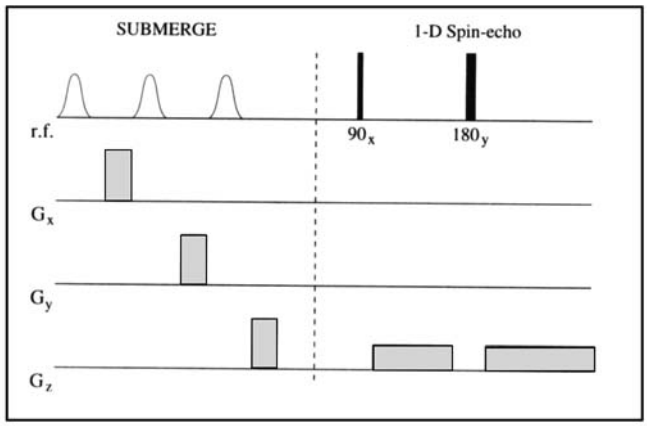

Figure 1. Pulse sequence used in the imaging experiments.

The SUBMERGE technique is comprised of three narrow-band (soft) RF pulses that selectively excite the resonance that is not of interest. The gradient, which is applied immediately after each RF pulse, "spoils" the component of the magnetization moment vector associated with that dimension. After three pulses, the resonance that is not of interest will be almost completely destroyed, and the standard 1-D spin-echo pulse sequence will image only the single resonance of interest.

Models of the Remediation Process

When an NAPL is introduced into the saturated zone of groundwater, it becomes trapped as small ganglia that cannot be removed by further displacement. If it is assumed that both the solid phase and the NAPL in the porous medium are stationary, the system consists of a flowing, continuous aqueous phase, which contains small amounts of dissolved contaminant and a discrete, stationary organic phase, which is slowly dissolving into the aqueous stream and losing volume. Neglecting surface interactions between the phases and spatial variation of porosity within the bed, the one-dimensional advection-dispersion equation for the water in the aqueous phase can be written:

$$n\rho_w\frac{\partial}{\partial t}(S_w\mu_w)+n\rho_w\frac{\partial}{\partial x}(v_xS_w\mu_w) - n\rho_wD_w\frac{\partial}{\partial x}\left(S_w\frac{\partial\mu_w}{\partial x}\right)=0. \quad (7)$$

For the dissolved contaminant in the aqueous phase, the transport equation is therefore

$$n\rho_w\frac{\partial}{\partial t}(S_w\mu_o)+n\rho_w\frac{\partial}{\partial x}(v_xS_w\mu_o) - n\rho_wD_w\frac{\partial}{\partial x}\left(S_w\frac{\partial\mu_o}{\partial x}\right)-E=0, \quad (8)$$

where n is porosity; ρ_1 is the density of phase i; S_i is the saturation or volume fraction of phase i with respect to the pore space; μ_i is the mass fraction of the species i in the aqueous phase; v_x is the mean pore velocity of the aqueous phase in the x-direction; D_i is the dispersion coefficient for species i; E is the rate of mass-transfer between the two liquid phases; and the subscripts w and o signify water and the organic contaminant, respectively. The equation for the dissolution of the NAPL is then

$$n\rho_o\frac{\partial}{\partial t}(S_o)+E=0. \quad (9)$$

In this system, all pores are filled with either the aqueous phase or the NAPL, and the aqueous phase is comprised of only water and contaminant. These two constraints can be written:

$$S_w+S_o=1 \quad (10)$$

$$\mu_w+\mu_0=1. \quad (11)$$

Since Eqs. 7–11 contain only four unknowns (S_w, S_o, μ_w, and μ_o), all five equations cannot be independent, and we may neglect one. The spatial dependence of v_x, the mean pore velocity at position x, is a direct function of the saturation of the aqueous phase:

$$v=v_xS_wn \qquad \text{constant for all } x, \quad (12)$$

where v is the superficial Darcy velocity. Hence, by using Eq. 11 to remove the explicit appearance of μ_w, substituting Eq. 12 for v_x, defining C_o to be $\mu_o\rho_w$ (the mass-concentration of contaminant in the aqueous phase), and rewriting the mass-transfer function as $F=E/n$ (thus characterizing the mass-transfer per volume of void space rather than volume of the system), Eqs. 8 and 9 become

$$\frac{\partial}{\partial t}(S_wC_o)+\frac{v}{n}\frac{\partial}{\partial x}(C_o)-D_w\frac{\partial}{\partial x}\left(S_w\frac{\partial C_o}{\partial x}\right)-F=0 \quad (13)$$

$$\rho_o\frac{\partial}{\partial t}(S_o)+F=0. \quad (14)$$

Further, by eliminating S_w with Eq. 10 and applying the chain rule to the dispersive term, Eq. 8 can be rewritten as

$$\frac{\partial}{\partial t}[(1-S_o)C_o]+\frac{v}{n}\frac{\partial}{\partial x}(C_o) - D_w\left[-\frac{\partial S_o}{\partial x}\frac{\partial C_o}{\partial x}+(1-S_o)\frac{\partial^2C_o}{\partial x^2}\right]-F=0. \quad (15)$$

The 1-D model representing the NAPL/groundwater system is completely described by Eqs. 14 and 15. The development of these two equations is entirely general with respect to F. These equations can be numerically evaluated for various functions F, and can therefore be used to test the results of various models.

In this work, the coupled partial differential equations, Eqs. 14 and 15 were evaluated using a staggered leapfrog finite difference technique (Press et al., 1992). The initial conditions of the finite difference scheme were chosen as follows:

$$C_o|_{x\geq 0}=C_s \quad (16)$$

$$S_o|_{x\geq 0}=\Phi_0(x), \quad (17)$$

where C_s is the equilibrium concentration of NAPL in water and $\Phi_o(x)$ is the initial saturation profile as determined from NMR data. The following boundary conditions are also applied:

$$C_o|_{x<0} = 0 \tag{18}$$

$$\left.\frac{\partial C_o}{\partial x}\right|_{x=L} = 0, \tag{19}$$

where L is the length of the column.

We now consider three physical models for the mass-transfer function, F, before comparing the results of the predictions of these models to the results of the NMR imaging experiments. Each model discussed here has been formulated such that the function F is described by only one free parameter.

Model 1: linear mass-transfer model

The first model described is the linear driving force model, which has been used by Powers et al. (1992) to evaluate the steady-state mass-transfer coefficient characterizing NAPL dissolution. In this model, F can be written simply as

$$F(S_o, C_o) = k_1 a(C_s - C_o) \tag{20}$$

where k_1 is the mass-transfer coefficient, a is the surface-area to volume ratio, and C_s is the equilibrium value for NAPL in water. Since k_1 and a are both unknown, it is both traditional and necessary by our single-parameter criterion that they be multiplied to give the single value, η_1, such that:

$$F(S_o, C_o) = \eta_1(C_s - C_o). \tag{21}$$

Model 2: pore-diffusion model

A second model, proposed by McDonald et al. (1993), assumes that the rate of mass transfer into the bulk aqueous phase is limited by the time of diffusion of the contaminant along a stagnant water region inside a pore neck as shown in Figure 2. As the dissolution occurs, the interface recedes into the pore, lengthening the diffusion path and reducing the mass-transfer rate. If the diffusion along a cylindrical pore is at a pseudo-steady-state, the flux of the NAPL will be given by

$$N_o = \frac{D_{o,w}}{\delta}(C_s - C_o), \tag{22}$$

where ρ_b is the population density of NAPL ganglia and a_b is the area available to mass transfer per ganglion. To obtain representation by assuming that all interfacial area available for mass-transfer is of this type, and so it may be written:

$$F(S_o, C_o) = \rho_b \frac{D_{o,w}}{\delta} a_b(C_s - C_o), \tag{23}$$

where ρ_b is the population density of NAPL ganglia and a_b is the area available to mass transfer per ganglion. To obtain

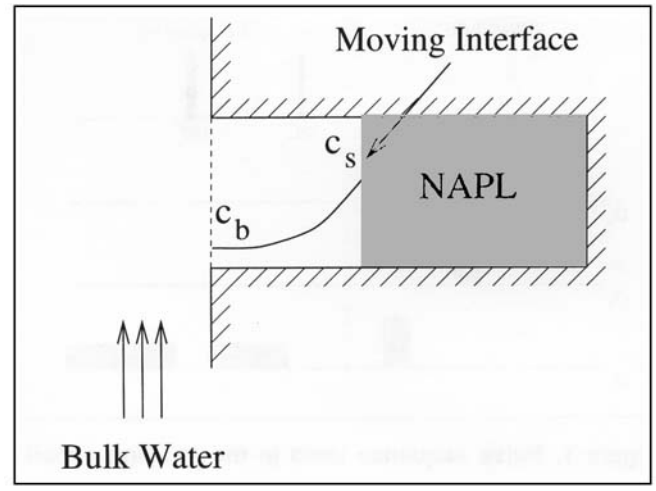

Figure 2. Idealized pore in the pore-diffusion model.

Each NAPL blob is trapped in a group of connected pores. As the NAPL dissolves, the interface recedes along the pore, lengthening the stagnant water region in the pore between the interface and the flow of bulk water. The NAPL that has dissolved at the interface must diffuse through this stagnant film before it joins the bulk water.

a form of Eq. 23 that is explicit for S, the following relationship is noted:

$$\rho_b = \frac{S_o^*}{V_b}, \tag{24}$$

where S_o^* denotes the initial saturation of NAPL and V_b is the initial volume for a single blob. Conrad et al. (1992) found that blob size is clearly related to the particle size characteristic of the porous medium. If this relationship is taken to be linear and solid particles are assumed to be spherical, then:

$$V_b = \frac{4}{3}\pi r_p^3 \nu, \tag{25}$$

where r_p is the mean particle radius and ν is a factor that relates the volume of a blob to that of a particle. Following from the work of Conrad et al. (1992), ν can be estimated to fall between 0.1 and 10. If the blob is assumed to be a sphere, but not all of the surface area is available for mass transport (i.e., it is either directly contacting the solid or is contacting a wetting film for which there is no pathway to the bulk aqueous phase), a_b can be written as

$$a_b = 4\pi r_p^2 \nu^{2/3} \alpha, \tag{26}$$

where α is the fraction of surface area available for mass transfer that will be less than unity and typically of order 0.1. Thus, the term $\rho_b a_b$ can also be written as

$$\rho_b a_b = \frac{3S_o^*}{r_p}\eta_2, \tag{27}$$

where $\eta_2 = \alpha \nu^{-1/3}$. Given the estimates for both α and ν, η_2 is expected to take a value between 0.05 and 2. Assuming

that a_b is constant over time and that initially there was no diffusion resistance (δ is zero when no NAPL has dissolved), a change in blob volume, ΔV, would equal δa_b so the diffusion path length can be written in terms of S_o:

$$\delta = \frac{\Delta V}{a_b} = \frac{S_o^* - S_o}{\rho_b a_b}. \tag{28}$$

Finally, combining Eqs. 23, 27 and 28, we obtain

$$F(S_o, C_o) = \left(\frac{3S_o^* \eta_2}{r_p}\right)^2 D_{o,w}\left(\frac{C_s - C_o}{S_o^* - S_o}\right), \tag{29}$$

where η_2 is the only free parameter in the model.

Model 3: shrinking-core model

Geller and Hunt (1993) propose treating NAPL dissolution as a case of spheres shrinking in a porous bed. Their analysis begins by assuming that Eq. 20 holds locally for NAPL ganglia that are spherical in shape. As the dissolution takes place, the NAPL spheres slowly shrink without being displaced axially, as illustrated in Figure 3. The surface area available for mass transfer, a, varies over the course of the experiment and is associated with the blob population density, ρ_b, by:

$$a = 4\pi r^2 \rho_b, \tag{30}$$

assuming that all blobs have the same radius, r. The number of blobs is assumed to be constant with changes allowed only in their size. Thus, ρ_b can be related to the initial saturation level by:

$$\rho_b = \frac{S_o^*}{\frac{4}{3}\pi r^{*3}}, \tag{31}$$

where r^* is the initial blob radius. The assumed geometry also allows us to relate the saturation to the radius of the blob after some dissolution has taken place:

$$S = S_o^*\left(\frac{r}{r^*}\right)^3. \tag{32}$$

Following Geller and Hunt (1993), who used a mass-transfer coefficient correlation for k_1 presented for dissolution of benzoic acid spheres (Wilson and Geankoplis, 1966):

$$k_1 = \frac{0.687}{n} v^{1/3}\left(\frac{D_{o,w}}{r}\right)^{2/3} \tag{33}$$

and combining Eqs. 20, and 30–33, a final expression for the model is obtained:

$$F(S_o, C_o) = \frac{2.06}{n} v^{1/3} D_{o,w}^{2/3} \eta_3 (S_o^*)^{5/9} S_o^{4/9} (C_s - C_o), \tag{34}$$

where η_3 equals $(r^*)^{-5/3}$ and is the fitting parameter.

The general characteristics associated with these three models are shown in Figures 4 and 5. The comparison of the dependence of mass-transfer rate on saturation is shown in Figure 4, and the characteristic trends in the evolution of NAPL saturation along a vertical column, given an initial NAPL saturation of 20% uniformly along the length of the column, for a Darcy velocity of 3.18 cm/hr are shown in Figure 5.

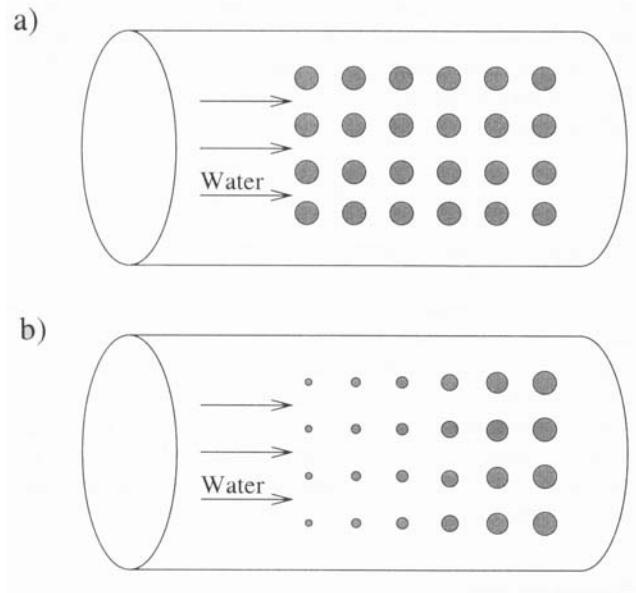

Figure 3. Mechanism of NAPL dissolution as described by the shrinking-core model.

(a) The NAPL begins as uniform spherical blobs that are evenly distributed throughout the column. (b) As the blobs begin to dissolve, they remain as discrete spheres, but their diameter is reduced.

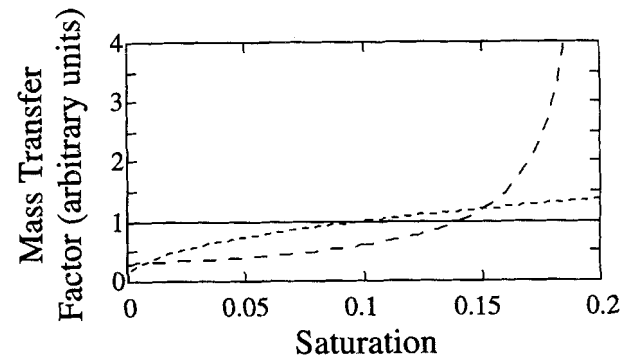

Figure 4. Comparison of the dependence of mass-transfer rate on saturation for the three models.

While the linear mass-transfer coefficient model (——) has no saturation dependence, the pore-diffusion model (----) and the shrinking core model (– – –) clearly show the effect of saturation upon mass transfer. The curves above were calculated using an initial saturation of 0.20 and were normalized such that the time required to reduce the saturation from 0.20 to 0.0 was constant.

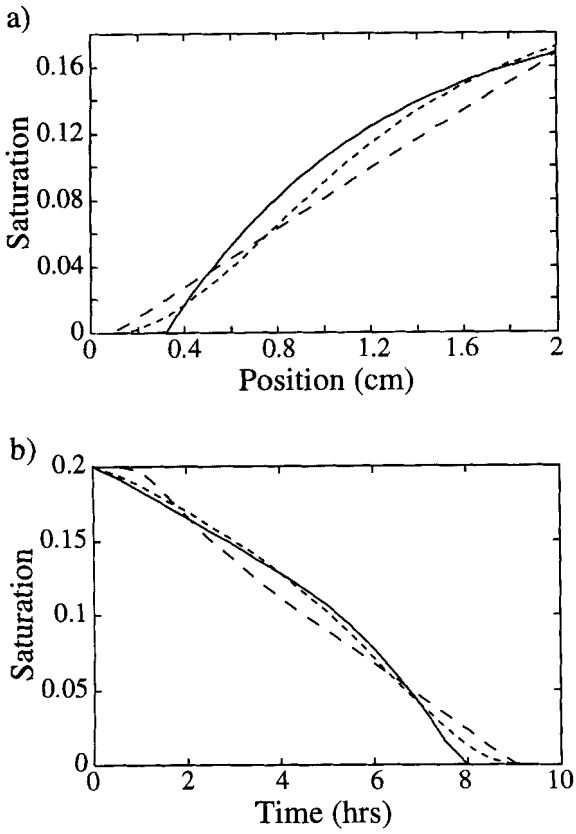

Figure 5. Trends in the evolution of NAPL saturation along a vertical column, given an initial NAPL saturation of 20% uniformly along the length of the column, for the linear mass-transfer coefficient model (——); the pore diffusion model (----); and the shrinking-core model (---).

A Darcy velocity of 3.18 cm/h is assumed. (a) NAPL saturation as a function of position from the bottom of the column at time 5 h after the start of dissolution. (b) NAPL saturation as a function of time at a position 1.02 cm from the bottom of the column.

Experimental Design

The NMR imaging experiments were performed using a Bruker Spectrospin MSL 200 NMR spectrometer with a field strength of 4.77 T and a ^{1}H microimaging probe fitted with an imaging coil of diameter 2.5 cm. The sample to be imaged was contained in a vertical column with an interior diameter of 2 cm and a height of 2 cm. The porous medium used was a high-purity sand, chosen for both its realistic particle size (74–354 μm in diameter) and its low concentration of paramagnetic ions. A low concentration of paramagnetic species is a requirement of the NMR technique, since the presence of such species causes spectral broadening in the frequency domain, as discussed earlier, which can make resolution of an aqueous resonance and an organic resonance separated by $\sim$ 700 Hz (at this magnetic field strength) impossible. The sand bed was created by allowing sand to settle into a water-containing column. The bed was supported by a sintered glass disk that was impermeable to the organic phase. The top of the sample cell was formed with a glass tube with a sintered glass disk attached to the end and was sealed with a Viton O-ring.

The NAPL studied in this work was *n*-hexanol; this hydrocarbon was chosen because of its intermediate solubility in water (0.11 mol %) (Sørenson and Arlt, 1979), which allowed the NAPL to be removed an order of magnitude faster than benzene or toluene, which are more typically used as contaminants in experiments and have a much lower solubility. The NAPL was forced into the water-saturated bed through the top of the column via a syringe pump at a Darcy velocity of 1.3 cm/h. The progression of the NAPL was monitored, and when the image indicated NAPL near the lower limit of the bed, the pump was switched and water was pushed into the column from below at the same Darcy velocity of 1.3 cm/h. The NAPL partially receded during this imbibition before the residual saturation of NAPL was reached and the dissolution process commenced. Water was flushed through the bed at rates in the range of 0.64–6.4 cm/h, and the NAPL was imaged at various times during the PT process. The experiment was stopped after several hours had elapsed without any detectable change in the saturation profile.

NMR Experimental Method

A 1-D spin-echo pulse train was used to image the column in three ways for each measurement. For two measurements, one of the aqueous phase and one of the NAPL phase, the pulse train was preceded by a SUBMERGE pulse sequence (Doddrell et al., 1986) to eliminate signal from all except the resonance of interest. One measurement was also taken without the SUBMERGE sequence to monitor any variations in the performance of the NMR spectrometer during the experiment. The images were acquired such that the 2 cm of active column length was resolved into 50 pixels.

Spin-lattice relaxation attenuation effects were minimized by using a recycle delay of greater than $5T_1$ between each successive scan. T_2 relaxation was accounted for by repeating the imaging experiments using different echo times, TE, and then fitting the resulting T_2-weighted profiles to the empirical equation,

$$I = I_0 \exp(-TE/T_2), \tag{35}$$

where I is the pixel intensity associated with a given TE, and I_0 is the pixel intensity as TE approaches 0. Chen et al. (1993) found that a biexponential form of Eq. 35 fitted their data statistically better than a single exponential expression. In the experiments reported here, the pore sizes were much larger than in Chen et al.'s rock sample; thus, a single fit (representing approximately uniform T_2 values for the organic phase throughout the pore structure) proved sufficient. Each measurement was taken at eight different echo times ranging from 3.2 ms to 50 ms.

Data Analysis

The images were analyzed on a Sun SPARC IPX workstation using in-house software. The images were fitted to Eq. 35 following linearization of the equation by performing a weighted least squares regression. Errors were calculated from the signal-to-noise ratio of each separate image, taking

into account the Rician distribution of white noise that has been magnitude-corrected as required in the image analysis (Whalen, 1971). The error analysis relied upon the approximation that the logarithm of a Rician distribution can be approximated by a Gaussian distribution. The resulting T_2-corrected images and the calculated errors were filtered to remove all values that resulted from a fit with lower than 80% probability of correlation. All points accepted were above the 95% confidence limit; thus eliminating any T_2 effects from the data used in the model fitting. The pixel intensities from the NAPL image meeting this criterion were divided by the appropriate pixel intensity values measured from the nonselective image of water in the porous medium at the start of the experiment, and then scaled by the difference in spin-per-volume ratio of the NAPL and water to provide saturation profiles of the NAPL. This procedure removes the effects of inhomogeneous coil response and the effects of B_1 inhomogeneities at the ends of the RF coil. Fits were performed on eight separate profiles for each experimental time step, and showed reproducibility to a precision of 0.02 in saturation.

The saturation profiles and error estimates were used to perform a weighted chi-squared fit of all three models using the merit function:

$$\chi_n^2(\eta_n) = \sum_{i=1}^{N} \left(\frac{\Phi_i - S_{n,i}}{\sigma_i} \right)^2, \qquad (36)$$

where the subscript n denotes the model used, $S_{n,i}$ is the predicted value of the NAPL saturation at point i for model n, Φ_i is the MRI saturation data at point i, and σ_i is the error estimate of point i. The merit function was minimized for each model and experiment. The minimum value for χ^2 was evaluated for goodness-of-fit using the incomplete gamma function. In the calculations reported below, the mean particle size of the sand used was 0.0225 cm and a bed porosity of 0.475 was assumed, as estimated from NMR data. n-Hexanol has a density of 0.8136 gcm^{-3} and a diffusivity in water of 0.021 cm^2/h; the latter value was estimated using methods described by Reid and Sherwood (1958).

Results and Discussion

The aim of this article is to highlight the use of NMR imaging in probing the mechanism of groundwater remediation. Figure 6 shows four of the saturation profiles for the n-hexanol experiment conducted under conditions of Darcy velocity of 3.18 cm/h. The profiles predicted by each of the three models outlined earlier are also shown. The typical error in the NAPL saturation measurement is ± 0.02, and therefore any apparent oscillations in the data are not considered to be significant. The profiles are both reproducible and show a consistent time-evolution within this precision. It is expected that fluctuations in the saturation profile will correlate with local fluctuations in pore structure and voidage; this is the subject of ongoing studies and will be discussed later. It is seen that all three models tend to underestimate the rate of removal of NAPL along the NAPL front at the beginning of the extraction. Visual comparison of the experimental data with the predictions from the three models suggests that the pore-diffusion model yields the most accurate description of the experimental data.

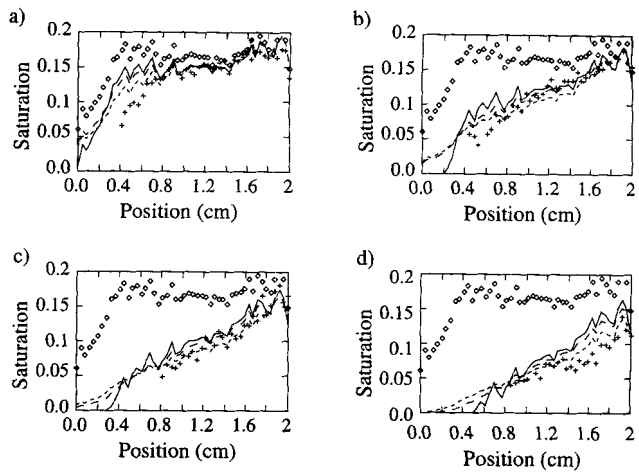

Figure 6. Selected profiles for the experiment performed using n-hexanol as the NAPL, and a Darcy velocity of 3.18 cm/h.

The residual saturation (◇◇◇◇) is shown on each graph for comparison. The results of the linear mass-transfer model (——), the pore-diffusion model (- - - -), and the shrinking-core model (— — —) are compared to the saturation data points (+ + + +) for four time intervals (h) during the experiment: (a) 1; (b) 2.6; (c) 3.6; (d) 4.6. Position indicates the distance (cm) from the bottom of the column. The time intervals correspond to the following equivalent pore volumes of water being flushed through the bed (a) 3.4; (b) 8.7; (c) 12.0; (d) 15.4.

Table 1 summarizes the results of the model-fitting study; the parameter values corresponding to the minimum χ^2 for all experiments and models are presented. It is immediately apparent from Table 1 that the model fits at larger Darcy velocities are superior to the fit for a Darcy velocity of 0.64 cm/h and that the fitted parameter η varies systematically with Darcy velocity independent of the model. Therefore, as we discuss in more detail below, the models fail to account for a strong dependence on Darcy velocity. However, for a particular velocity we can still use the results shown in Table 1 to indicate which model of the dissolution process best fits the data. For each flow velocity considered it is clearly seen that the linear mass-transfer model gave the poorest agreement with experimental data, while the pore-diffusion model more closely fitted the experimental data than did the shrinking-core model. Other results are also obtained directly from

Table 1. Results of the Modeling Study*

NAPL	Darcy Vel. cm/h	Model	η	χ^2
n-hexanol	0.64	1	1.84	3,560
		2	0.083	2,280
		3	32.2	3,010
n-hexanol	3.18	1	7.10	266
		2	0.191	125
		3	80.6	183
n-hexanol	6.37	1	22.4	238
		2	0.321	102
		3	208	178

*The experimental data have been fitted to three models, each containing only one unconstrained parameter: Model 1—the linear mass-transfer model; Model 2—the pore-diffusion model; and Model 3—the shrinking-core model. The goodness-of-fit parameter χ^2 is calculated as defined in Eq. 36.

the data given in Table 1. First, the value of the fitting parameter, η, obtained from the pore-diffusion and shrinking-core analysis (Models 2 and 3) are expected to fall within a well-defined region. For the pore diffusion model, η falls between 0.05 and 2 as predicted, while the results of the shrinking-core analyses provide an estimate of initial ganglion radius of between 0.4 mm and 1.3 mm. The estimate of ganglion size obtained here is consistent with the work of Conrad et al. (1992), who reported that NAPL ganglia tend to be larger than, but of the same order of magnitude as, the sand particles forming the packed column. Model fits to the data corresponding to different Darcy velocities, v, indicated a strong dependence of the fitting parameter, η, on v, and hence a strong variation of mass transfer with Darcy velocity. Such a strong dependence, which scales approximately as $v^{0.9 \pm 0.2}$, is not predicted by any of the models. Indeed, at the lowest Darcy velocity the model fits are considerably worse, indicating a failure of all models to predict the dissolution behavior in this limit. Only the shrinkage-core model predicts a v-dependence, and in this case the dependence scales as $v^{1/3}$. This is a highly interesting result for PT remediation schemes. Given that the earlier work of Wilson and Geankopolis (1966) reported a mass-transfer coefficient that scaled as $v^{1/3}$ for the case of dissolution of benzoic acid spheres, it seems quite sensible that this related system should exhibit mass transfer that has a power-law dependence on flow rate. While the results presented in this work are not caused by imaging or modeling artefacts, the relatively limited number of experiments and velocity range studied in this work advise caution against an overambitious interpretation of these preliminary data. If these initial findings are confirmed to be valid over a wide range of process conditions, the results will have implications for a real cleanup situation; any dependence on Darcy velocity introduces a competition between the cost and speed of a PT remediation treatment in the field.

The reason for the success of the pore-diffusion model can be understood with reference to Figure 4, which shows that the pore-diffusion model predicts extremely fast removal at NAPL saturation levels near the residual saturation. The NAPL dissolution rate then decreases rapidly as the saturation decreases and remains almost constant once the saturation has reached half that of the initial saturation. Figure 7 shows the correlation between the experimental determination of NAPL saturation obtained from NMR imaging and the values of NAPL saturation predicted by the pore-diffusion model. It is seen that errors are randomly placed with respect to NAPL saturation.

Future experiments will be performed on a 4.5-cm-diameter column, thereby minimizing wall effects and providing a larger imaging volume that will, in turn, increase signal to noise in these studies. In particular, studies will focus on data acquisition at long times during the remediation process when the NAPL saturation is low. These data will allow us to discriminate more clearly between the three models discussed here. For example, Figures 6c and 6d clearly demonstrate that the prediction of the linear mass-transfer model deviates strongly from the trends predicted by the pore-diffusion and shrinking-core models at long remediation times. However, data acquisition in this regime is associated with experimental difficulties. As the NAPL saturation decreases the ability

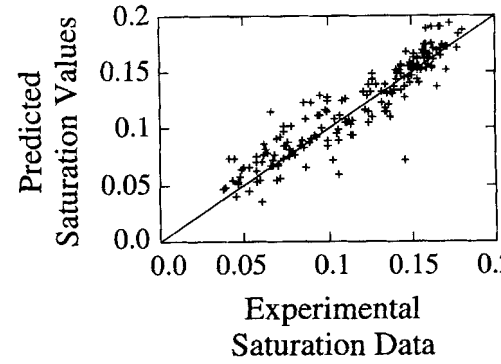

Figure 7. Scatter plot of the predictions of the pore-diffusion model compared with experimental data acquired at a Darcy velocity of 3.18 cm/h.

For each experimental data point—for all times and at all measured locations within the column—the experimental value is compared to the value predicted from the pore-diffusion model. The straight line indicates a perfect fit of the model to the data.

to record reliable NMR imaging data also decreases as a result of increasing T_2 contrast effects. In the present study, the T_2 relaxation time constant was approximately 20–30 ms for values of the NAPL saturation greater than 7%, but decreased with decreasing NAPL saturation down to values of ~ 10 ms for saturations of 5%. Although this contrast can be removed as described earlier, T_2-corrected NAPL saturations are not quoted for values lower than 2.5%, since at these low saturations corrections for relaxation contrast, from which estimates of the saturation are obtained, contain significant error. In ongoing studies we are using NMR imaging to investigate correlations of voidage characteristics (pore shape and particle size), NAPL, and surface properties of the particles, with ganglion size and remediation mechanism. In the first instance, we are studying model systems in which the porous medium is represented by packings of 6-mm-dia. glass ballotini. Using this experimental configuration we are able to image individual ganglia as well as the detailed pore structure within the bed. The results of these studies will be used to probe the basic physics of two-phase transport and dissolution within a pore structure, in the light of which we will critically assess the applicability of the models presented here in describing NAPL dissolution. Any new insights will be incorporated into a modified model of NAPL dissolution and this new model will be compared with the data from sand-filled columns, such as are used in the work presented in this article. A detailed investigation of the relationship between pore structure and NAPL dissolution using NMR imaging cannot be applied directly to a sand-filled column. Such studies would require spatial resolution of the order of 50 μm. While such resolution can be achieved with NMR imaging, the experiment would need a far greater data-acquisition time. It is also noted that even with a spatial resolution of 50 μm, unambiguous characterization of the pore structure would be difficult.

Conclusions

NMR imaging can be used to noninvasively quantify NAPL saturation in an experimental column. The results of this ex-

periment suggest that at higher Darcy velocities the pore-diffusion model best describes PT remediation in a homogeneous porous medium. It also indicates that the shrinking-core model produces considerably better results than the less complicated linear mass-transfer coefficient model. The estimate of ganglion size from the shrinking-core model and the fitting parameter in the pore-diffusion model were within the range expected when compared with the results of other workers. However, none of the models predicted the observed dependence of mass transfer upon Darcy velocity, and this is most evident from the poor agreement between models and experiment at the lowest Darcy velocity investigated. Until this effect can be accurately measured and accounted for, all of the modeling schemes considered here will fail to predict mass transfer in an NAPL-contaminated system.

Acknowledgments

C. A. Baldwin thanks the British Marshall Commission for the award of a Marshall Scholarship. L. F. Gladden thanks the EPSRC for providing funding for the NMR spectrometer and Zeneca for the award of a Zeneca Fellowship. We also wish to thank P. Alexander for providing the in-house image analysis software.

Notation

D = dispersion coefficient
$D_{o,w}$ = diffusivity of NAPL in aqueous phase
M = magnitude of the bulk magnetic moment
N = number of experimental data points
t = time
T_1 = spin-lattice relaxation time constant
T_2 = spin-spin relaxation time constant
x = position along length of column
ρ = fluid density
χ^2 = weighted residual sum of the squares

Literature Cited

Borden, R. C., and C. M. Kao, "Evaluation of Groundwater Extraction for Remediation of Petroleum-Contaminated Aquifers," *Water Environ. Res.*, **64**, 28 (1992).

Callaghan, P. T., *Principles of Nuclear Magnetic Resonance Microscopy*, Clarendon Press, Oxford (1991).

Chen, S., F. Qin, K.-H. Kim, and A. T. Watson, "NMR Imaging of Multiphase Flow in Porous Media," *AIChE J.*, **39**, 925 (1993).

Conrad, S. H., J. L. Wilson, W. R. Mason, and W. J. Peplinski, "Visualization of Residual Organic Liquid Trapped in Aquifers," *Water Resour. Res.*, **28**, 467 (1992).

Doddrell, D. M., G. J. Galloway, W. M. Brooks, J. Field, J. M. Bulsing, M. Irving, and H. Baddeley, "Water Signal Elimination in Vivo, Using Suppression by Mistimed Echo and Repetitive Gradient Episodes," *J. Magn. Reson.*, **70**, 176 (1986).

Fordham, E. J., L. D. Hall, T. S. Ramakrishnan, M. R. Sharpe, and C. Hall, "Saturation Gradients in Drainage of Porous Media: NMR Imaging Measurements," *AIChE J.*, **39**, 1431 (1993).

Freeze, R. A., and J. A. Cherry, "Guest Editorial—What Had Gone Wrong," *Ground Water*, **27**, 458 (1989).

Geller, J. T., and J. R. Hunt, "Mass Transfer from Nonaqueous Phase Organic Liquids in Water-Saturated Porous Media," *Water Resour. Res.*, **29**, 833 (1993).

Gladden, L. F., "Nuclear Magnetic Resonance in Chemical Engineering: Principles and Applications," *Chem. Eng. Sci.*, **49**, 3339 (1994).

Imhoff, P. T., P. R. Jaffé, and G. F. Pinder, "An Experimental Study of Complete Dissolution of a Nonaqueous Phase Liquid in Saturated Porous Media," *Water Resour. Res.*, **30**, 307 (1993).

Majors, P. D., J. L. Smith, F. S. Kovarik, and E. Fukushima, "NMR Spectroscopic Imaging of Oil Displacement in Dolomite," *J. Magn. Reson.*, **89**, 470 (1990).

Mansfield, P., and P. K. Grannell, "NMR 'Diffraction' in Solids," *J. Phys. C.*, **6**, L422 (1973).

McDonald, J. P., C. A. Baldwin, L. E. Erickson, and L. T. Fan, "Modeling Bioremediation of Soil Aggregates with Residual NAPL Saturation," *Proc. Conf. on Hazardous Waste Res.*, Kansas State Univ., Manhattan, p. 346 (1993).

Powers, S. E., L. M. Abriola, and W. J. Weber, Jr., "An Experimental Investigation of Nonaqueous Phase Liquid Dissolution in Saturated Subsurface Systems: Steady State Mass Transfer Rates," *Water Resour. Res.*, **28**, 2691 (1992).

Press, W. H., S. A. Teukolsky, W. T. Vetterling, and B. P. Flannery, *Numerical Recipes in FORTAN: The Art of Scientific Computing*, Cambridge Univ. Press, Cambridge (1992).

Reid, R. C., and T. K. Sherwood, *The Properties of Gases and Liquids*, McGraw-Hill, New York (1958).

Roussel, J. C., and C. Chardaire-Riviere, "Use of High Magnetic Fields in the Visualization of Porous Media," *J. Chim. Phys.*, **89**, 325 (1992).

Sørenson, J. M., and W. Arlt, *Liquid-Liquid Equilibrium Data Collection 1: Binary Systems*, DECHEMA, Frankfurt (1979).

Whalen, A. D., *Detection of Signals in Noise*, Academic Press, New York (1971).

Wilson, E. J., and C. J. Geankopolis, "Liquid Mass Transfer at Very Low Reynolds Numbers in Packed Beds," *Ind. Eng. Chem. Fundam.*, **5**, 9 (1966).

Manuscript received Apr. 11, 1995, and revision received Aug. 4, 1995.